Journal of Instrumentation

SISSA

PAPER • OPEN ACCESS

Beam-induced electron multipacting with mode resonance in a vacuum chamber

To cite this article: H.J. Cha *et al* 2021 *JINST* **16** P11001

Published by IOP Publishing for Sissa Medialab

Received: *June 11, 2021*
Revised: *August 30, 2021*
Accepted: *September 9, 2021*
Published: *November 2, 2021*

Beam-induced electron multipacting with mode resonance in a vacuum chamber

---

H.J. Cha,[*] **D. Saez de Jauregui, A. Grau and A.-S. Müller**

Karlsruhe Institute of Technology,
Hermann-von-Helmholtz-Platz 1, Eggenstein-Leopoldshafen 76344, Germany

E-mail: `hyuk.cha@kit.edu`

Abstract: Some vacuum chambers in particle accelerators perform a waveguide- or resonator-like behavior due to their unique geometries. Electron multipacting caused by such a structural property might be able to overwhelm the classical beam-induced multipacting. This article shows that the wakefields of particle beams could stimulate the resonant modes of a vacuum chamber with a near-rectangular waveguide shape and accordingly induce much stronger electron avalanche in the chamber. Especially, it has been believed that the multipacting is responsible for pressure rise in a vacuum chamber, where energetic secondary electrons with growing numbers collide with gas particles at the chamber wall. Based on numerical simulations, the electron multipacting mechanism with the mode resonance is proposed, which can explain the significant pressure variation measured in our cryogenic vacuum chamber.

Keywords: Accelerator Subsystems and Technologies; Coherent instabilities

2021 JINST 16 P11001

---

[*] Corresponding author.

https://doi.org/10.1088/1748-0221/16/11/P11001

Contents

1 Introduction

In accelerator vacuum chambers, the formation of electron clouds could be one of the significant sources of beam-induced heat loads such as synchrotron radiation (SR), geometrical impedances, and resistive wall heating [1]–[7]. Furthermore, serious electron multipacting (MP), which means resonant electron discharge phenomena in materials with high secondary electron yield (SEY), with charged particle beams in the chambers have been also reported in literature with numerical simulations, direct measurements, and indirect observation of vacuum pressure rise [1, 8]–[10]. The beam-induced electron MP (BIEM), which gives rise to demerits of beam energy loss and chamber heating, is based on a mechanism that the electrons are kicked and multiplied by wakefields (WFs) of passing bunch trains [1, 10]. The electron MP phenomena are also commonplace in radiofrequency (RF) devices such as normal and superconducting cavities and fundamental power couplers [11]. From frequent surface impacts by synchronization of the initially emitted electrons with strong RF fields, the number of total electrons exponentially increases with time. Thus, it is obvious that the MP results in RF breakdown and finally limits the device performance. In general, the MP-possible areas are confined in small regions in the device structure and can be mitigated by geometrical design optimization [12]. The MP barriers restricting power supply to the devices have been also overcome by RF conditioning during several to tens of hours [13].

Figures 1(a) and 1(b) show simple principles of the BIEM with positively and negatively charged beams, respectively, in a vacuum chamber. The MP with the positively charged beams is superior to that with negatively charged ones due to the relatively stronger kinetic energy from attraction between the beams and the primary electrons from the chamber wall. On the other hand, one can consider the MP with resonant modes trapped in a vacuum chamber which acts like an RF device, as shown in figures 1(c) and 1(d). If the electromagnetic (EM) fields from the resonance are much stronger than those from particle beams, the BIEM will be buried under the MP with mode resonance where the more secondary electrons with higher energy will be created regardless of the

2021 JINST 16 P11001

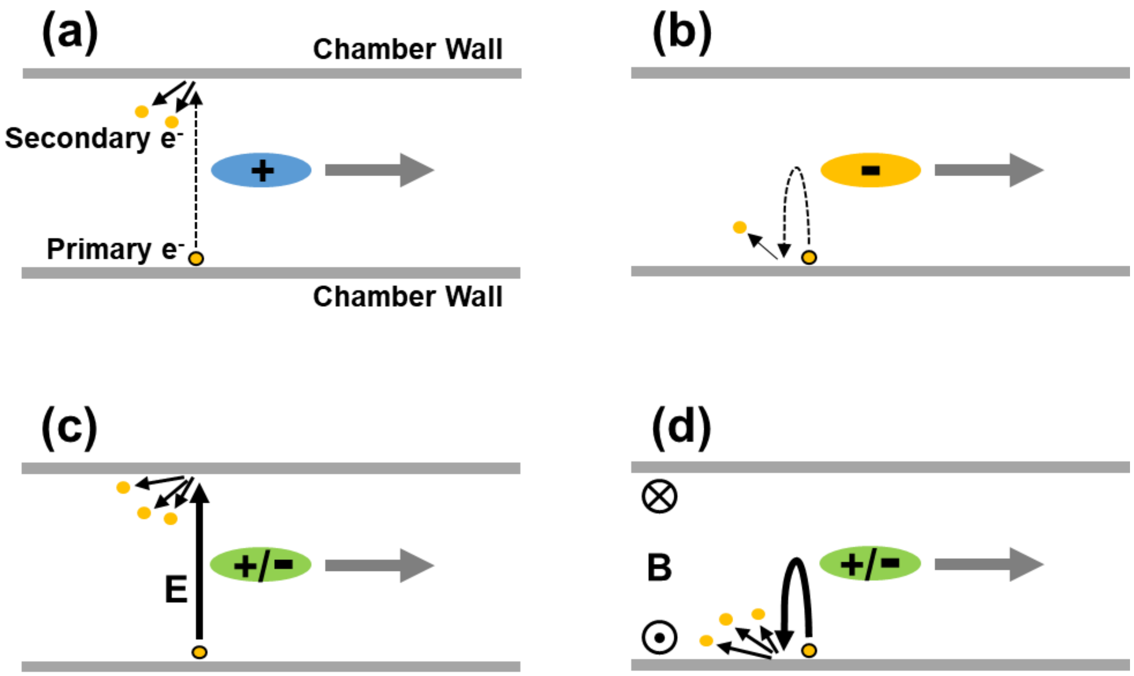

Figure 1. Schematics showing the beam-induced electron multipacting with (a) a positively charged beam [+], (b) a negatively charged beam [−] and with (c) electric field [E], (d) magnetic field [B] of mode resonance in a vacuum chamber.

charge gender. The dominant fields in the mode resonance are dependent on a unique structure of the chamber.

The pressure rise in a cold vacuum chamber with cryogenic environment may be a proof of strong MP because the energetic secondary electrons can repeatedly desorb the gas molecules cryosorbed in the chamber wall. An actual case was at Karlsruhe Institute of Technology (KIT), where the Karlsruhe Research Accelerator (KARA) electron storage ring has been operated with superconducting insertion devices such as wigglers and undulators [14]. Significant pressure variations were observed in a cold-bore vacuum chamber for a superconducting undulator with a period length of 14 mm (SCU14) when no magnetic fields were applied. The chamber in the SCU14 had a near-rectangular waveguide structure of two bended stainless steel (SS) substrates in upper and lower, on which each thin copper (Cu) layer was partially deposited around a beam direction to minimize the image current of the beam. The corresponding gas dynamic analyses demonstrated that electron MP was responsible for the pressure rise, but the related mechanism has not been clear [14].

It has been well informed that the BIEM severely occurs with positively-charged particle beams attracting the secondary electrons from the chamber surface [15]. For instance, some observations of pressure rise, as a result of the MP, with regard to a current of positron beams in the warm straight section of the PEP-II LER (positron-electron project-II low energy ring; nominal bunch length and spacing of ~40 ps r.m.s. and 8 ns, respectively; 1582 bunches in 24 trains, reported in 2004) have shown the abrupt growth whose threshold started at a current of around 600 mA and saturation (or decay) at a peak current of ~1.1 A [15]–[18]. The chamber material of the straight section with 4″

cylindrical beam pipes was SS [19]. In our case with electron beams in the KARA storage ring (bunch length and spacing of ~40 ps r.m.s. and 2 ns, respectively; 64 bunches in 2 trains, reported in 2007), the pressure variation measured with an average beam current indicated Gaussian-like distribution at the relatively lower peak current of around 150 mA, as shown in figure 2, even in the cold vacuum chamber at a temperature of 4 K, where the binding energies of physisorbed gas molecules were much higher than those in a warm condition [20]. A direct comparison is difficult, however, considering that the BIEM with negatively charged beams is inferior to that with positively charged ones, one could imagine in general that the pressure rise with the electron machine KARA should be maintained until or beyond much higher beam currents like the PEP-II LER cases, in contrast to the measurement results. Assuming that the vacuum pressure is linearly dependent on the MP, our results are similar to the MP band formation with regard to the EM fields in a resonant RF device with a specific structure.

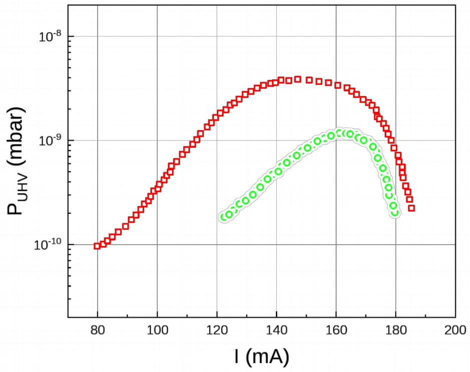

Figure 2. An example of vacuum pressure (P_{UHV}) variation with average beam current (I) measured at the KARA electron storage ring. The cold vacuum chamber of the SCU14 was tested without magnetic fields. Each curve corresponds to a different fill. Source: adapted from Casalbuoni et al. 2007 [20], figure 8.

Several research groups have investigated the trapped resonant modes in insertion devices and verified that vacuum chambers with mode resonance, for example, a resonant waveguide- or cavity-like chamber could give disturbance to nearby accelerator devices like a beam position monitor (BPM) [21]–[23]. It has been also reported that the resonant modes in a vacuum chamber could be caused by a charged particle beam [22, 24] and moreover, by a large resonance peak in transverse impedance of a chamber gap [25]. Such previous investigations allowed us to consider the mode resonance-assisted MP in vacuum chambers. This postulate will be also helpful to understand the MP phenomena and resultant pressure variation observed in vacuum chambers with electron machines such as the KARA.

The purpose of this study is to check out the possibility of reproduction of the nonlinearity in experimental results shown in figure 2 from numerical analyses. In the following sections, simulation results on strong MP assembled with mode resonance in a rectangular waveguide-like vacuum chamber are presented. It starts from a condition that dominant modes in the chamber are excited by WFs of particle beams. In order to prove the coherence between them, the wake spectra from a single bunch passing through the vacuum chamber were compared to the eigenmode frequencies of the resonant chamber. The MP with scaling the EM fields in a resonant mode, which correspond to a beam current in measurements, was also analyzed. Finally, a fundamental cause of the strong MP from the additional studies for chambers having different structure is discussed. The photoemission contribution to the MP by SR was not considered in this study.

2 Numerical analysis

From geometries of the SCU14, a virtual chamber was set to be a rectangular waveguide of 1-mm-thick SS with the inner dimensions of 66 mm (width) × 29 mm (height) × 1400 mm (length) for the following simulations, even though the real chamber has two Cu layers with a thickness of 30 µm and a width of ±10 mm from the horizontal center on the top and bottom SS substrates, respectively, and also partial absence of the side walls for ultrahigh vacuum.

2.1 Wakefield simulations

In order to confirm spectral coherence between electron bunch-induced WFs and resonant modes in the vacuum chamber, the WF analyses with the CST Particle Studio (PS) Wakefield Solver were performed at the very first. The material properties of the SS used in the simulations are summarized in table 1, which was introduced from commercial documents and ref. [26]. The number of meshes was more than 10^8 with a mesh volume of $0.34 \times 0.34 \times 0.34\,\mathrm{mm}^3$, which is enough for resolving the chamber modeling. For simplicity of the simulation, we supposed not bunch trains but a single bunch with a current of 1 mA and a length of 13.5 mm (45 ps). Table 2 shows the key parameters of the KARA electron beam, where the numbers in the last column indicate the values used in the analyses. The simulations was also performed with a temporal step of pico-second (ps) [27]. Figure 3(a) shows the single bunch spectrum where the maximum frequency reaches approximately 30 GHz. The variation of wake potential in longitudinal (z-) direction along the chamber length is shown in figure 3(b), where the red curve indicates a Gaussian reference pulse (electron bunch). The longitudinal wake potential oscillates in the entire distance, which means a narrow-band coupling impedance in a longitudinal wake spectrum and is also shown as resonance peaks in absolute values in figure 4(a). Both results indicate that the vacuum chamber behaves as a resonant waveguide due to its unique rectangular structure. Figure 4(b) shows real and imaginary parts of the longitudinal impedance, respectively. The squared cosine filtering with a roll-off factor of 0.5 was applied to all wake and impedance spectra for the visibility. The wake potentials and impedances in horizontal (x-) and vertical (y-) directions were zero, respectively, from the initial condition of on-axis beams. However, if the beam offsets (shifts) in transverse directions are given, the transverse wake characteristics grow up owing to the increasing kick factors, as shown in figure 5 where each 2 mm shift was applied in both x- and y-directions. The resonant frequencies in transverse spectra are almost coincident with those in the longitudinal one. There was no difference between longitudinal wake potentials and impedances with and without the wake shifts. As the RF frequency is 500 MHz, the WF simulation results imply that harmonic mode resonances exist in the vacuum chamber.

2.2 Electromagnetic simulations

The CST Microwave Studio (MWS) Eigenmode Solver was utilized to characterize EM fields in the vacuum chamber. Figure 6(a) shows the resonant frequencies in 10 modes by AKS method

Table 1. Material properties of the stainless steel used in the WF simulations.

Parameter	**Value**
Electric conductivity (S/m)	1.4×10^6
Material density (kg/m^3)	8000
Thermal conductivity at 300 K (W K^{-1} m^{-1})	16.2
Specific heat (J K^{-1} kg^{-1})	502
Diffusivity (m^2/s)	4×10^{-6}
Thermal expansion coefficient (10^{-6}/K)	17.3

Table 2. Key parameters of an electron beam in the KARA storage ring (E: electron energy, f_{rf}: RF frequency, f_{rev}: revolution frequency, σ_x: horizontal beam size, σ_y: vertical beam size, σ_z: bunch length, c: speed of light in vacuum, I: average beam current, N_b: number of bunches, and Q_b: bunch charge). The numbers in the last column (Value*) indicate the values used in the WF simulations.

Parameter	**Value**	**Value***
E (GeV)	0.5–2.5	—
f_{rf} (MHz)	500	
f_{rev} (MHz)	2.715	
σ_x, σ_y (mm, in r.m.s.)	0.84, 0.063	
σ_z/c (ps, in r.m.s.)	several to 50	45
I (mA)	≤ 200	100
N_b	1–184	100
Q_b (nC)	0.037–0.37	0.37

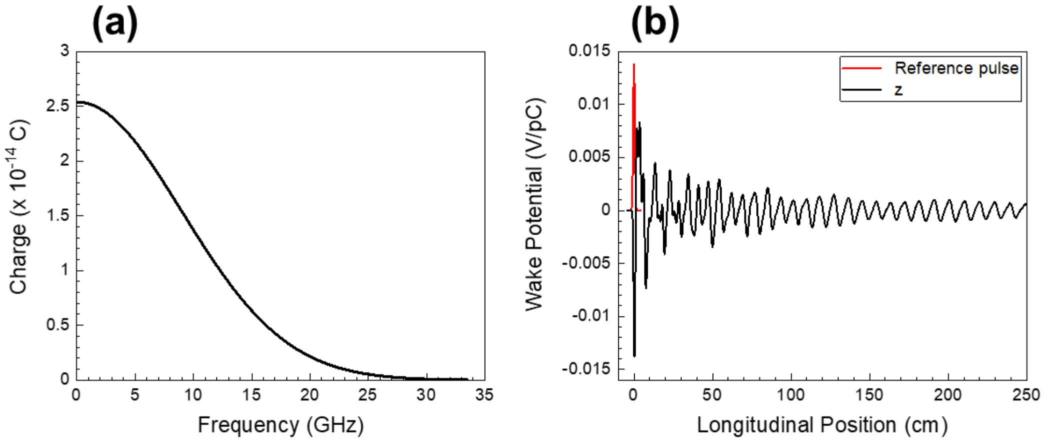

Figure 3. (a) A single bunch spectrum with a bunch length of 13.5 mm (45 ps) and a current of 1 mA and (b) variations of wake potential in longitudinal (z-) directions along the vacuum chamber length. The reference pulse indicates a Gaussian electron bunch.

(~10^7 meshes) and 64 modes by JDM method (~10^5 meshes), respectively [28]. The cut-off frequencies were ~2.3 GHz and the maxima were around 5 GHz in both methods. This frequency

2021 JINST 16 P11001

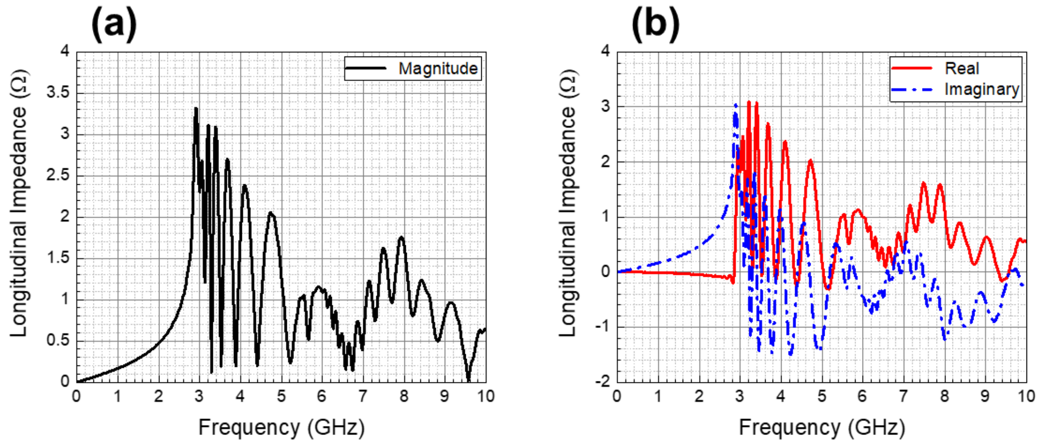

Figure 4. (a) Wake spectrum (absolute value) in longitudinal direction in the vacuum chamber and (b) its real and imaginary parts.

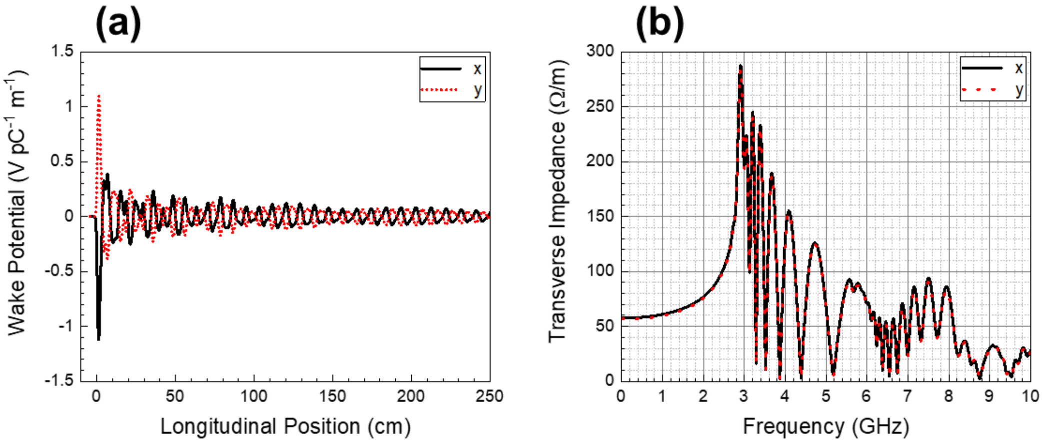

Figure 5. (a) Variations of wake potentials along the vacuum chamber length and (b) wake spectra (absolute values), in transverse directions with wake shifts of 2 mm in x- and y-directions, respectively.

ranges are well overlapped with resonant peaks in the longitudinal and transverse WF spectra in section 2.1. Thus, it is inferred that the mode resonances in the vacuum chamber (unloaded quality factor, $Q_0 = \sim 2 \times 10^3$ in fundamental modes at both 4 and 300 K) are caused by coherent WFs and the amplified EM fields can result in the electron MP. From the WF analyses, it seems that the longitudinal WF dominantly affects to the mode resonances. However, one cannot completely exclude the contribution by the transverse WF, considering the transverse impedance effects in the off-axis WF analyses and ref. [25]. Figure 6(b) shows variations of Q_0 and shunt impedance, R_{sh} with respect to a mode number calculated by the AKS method. Considering the real Cu layers partially deposited on the SS substrates, it is expected that the Q_0 would rise some amount. However, the increment is believed to be not so significant because the total surface area of the Cu is ~20% of that of the SS, even though a skin depth of ~250 nm in the Cu at the frequencies is much lower than its thickness of 30 μm. For reference, the Q_0 of a vacuum chamber made of only Cu is calculated to be ~30 times higher than that of the SS chamber at the temperature of 4 K. Unfortunately, the EM modeling with two hetero-materials of SS and Cu was not possible due to a prerequisite of a perfect conductor composed of a single material in the CST MWS code. Figure 7 shows the electric-field (E-field) distributions in four distinguishable modes, which represent typical transverse electric (TE) modes. As input parameters for the MP analyses in section 2.3, the EM fields at 2.3 GHz among the harmonic modes were chosen (figure 8). Even though one consider the actual case with partial Cu deposition in the horizontal walls, the magnetic field regions mainly belong to the vertical walls of SS, as shown in figure 8(c), which is much more dominant in the MP and will be described in the next section. The field values in the legends of figures 8(a) and 8(c) originated from an assumption that an energy of 1 J was stored in the vacuum chamber. Figure 8(b) shows the E-field distribution along the beam axis. The amplified EM fields can be calibrated by direct measurements in the chamber.

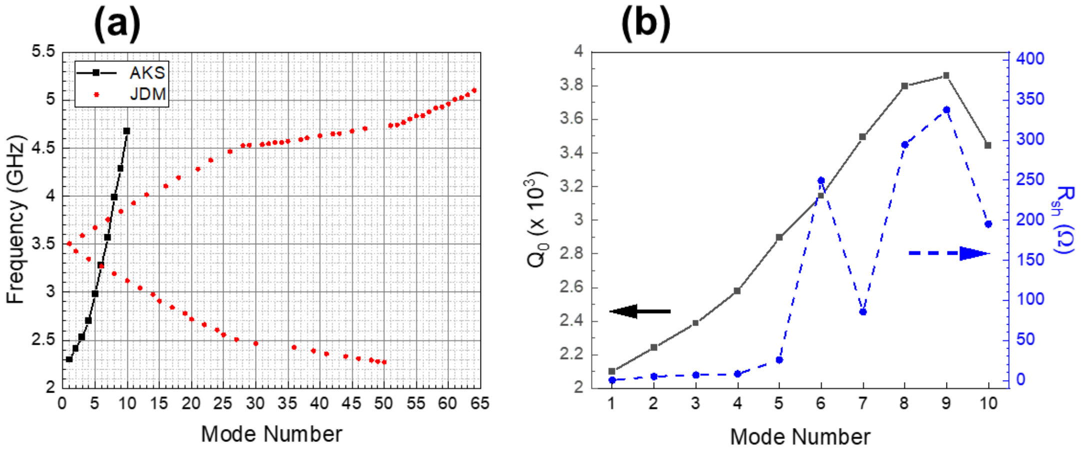

Figure 6. Variations of (a) resonant frequency calculated by AKS and JDM methods, respectively, and (b) unloaded quality factor, Q_0 and shunt impedance, R_{sh} by AKS method, with respect to a mode number in the vacuum chamber.

2.3 Multipacting simulations

The MP analyses were performed using CST PS PIC (particle in cell) Solver, where the code did not offer the SEY information for SS. However, it is known that SS has an SEY characteristics similar to that of Cu and the difference between the properties at room and cryogenic temperatures for such high SEY materials is not significant, especially, in low electron energies of less than ~100 eV [1, 29]. Thus, the SEY of pure Cu shown in figure 9(a) was inevitably applied to the MP simulations, which is basically offered in the CST PS code. Fortunately, figure 9(a) resembles the curve of SS in figure 9(b) which gives the SEY information of several material in the literature [1, 30]. For this reason, it is believed that the difference in the MP analyses between the Cu modeling and the real vacuum chamber with partial Cu layers on the SS substrates would be negligible.

Figure 10 shows the MP simulation results for the vacuum chamber. For a parameter sweep study with changing the EM fields corresponding to a beam current, the mesh number was set to $\sim 5.5 \times 10^5$ for each simulation with a mesh volume of $2.3 \times 1.1 \times 2.3\,\text{mm}^3$. The mesh dimension is enough for the analyses because the number of points for initial electron emission from the

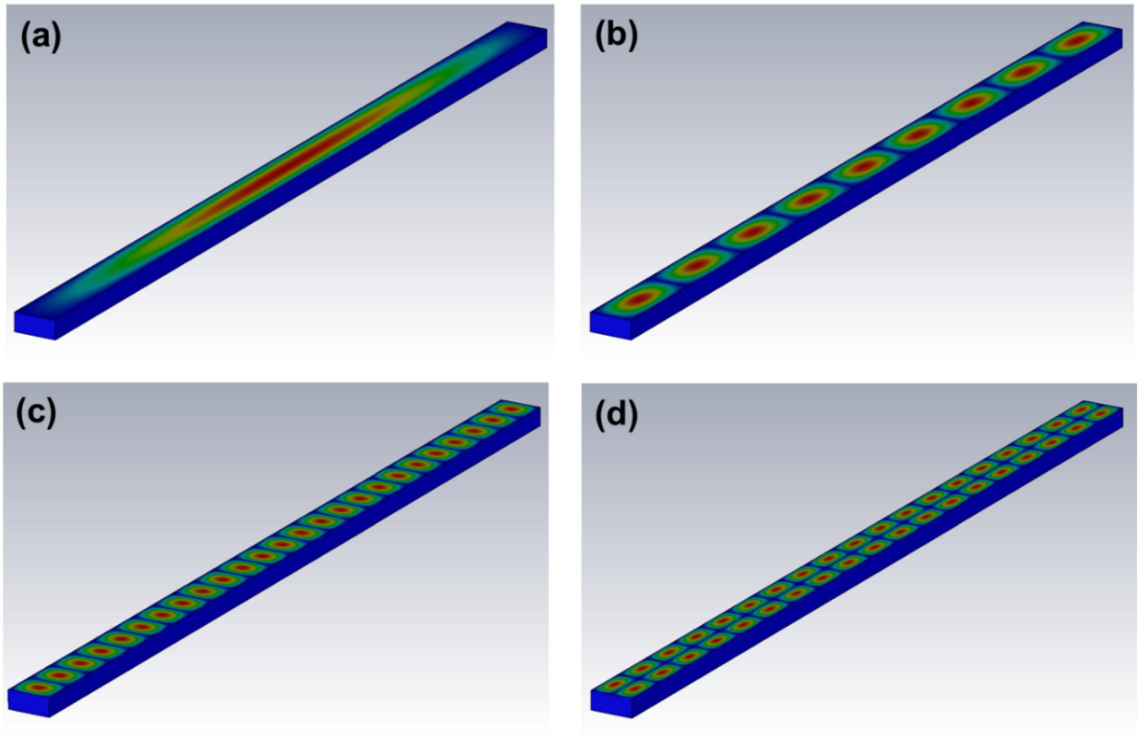

Figure 7. Electric field distributions in the vacuum chamber with resonant frequencies of (a) 2.27175 GHz, (b) 2.46529 GHz, (c) 3.50685 GHz, and (d) 4.96243 GHz, respectively. They represent typical TE modes.

four inner surfaces was supposed to only 80, as shown in the inset of figure 10(a), for distinctly monitoring the electron motion and the surface emission does not depend on the material thickness. It was also supposed that 4 Gaussian bunches with kinetic energies of 10 eV were emitted from each point in a time scale of nano-second (ns), which was the same as that in the EM simulations. The EM fields in figure 8 were imported for the analyses and scaled to investigate their dependency on the MP. The scaling factor of the EM-field intensity was denoted as κ in the legends of figure 10, which can also correspond to the average beam current, I in figure 2. Figure 10(a) shows typical exponential growth of total electron numbers with respect to time at certain κ's. In general, as the κ, namely, EM-field intensity, increases, the particle numbers start growing in time and then abruptly or gradually decrease after a critical κ. Otherwise, such rising and falling vanish from the beginning or can be repeated in different κ ranges owing to the characteristic structure of the vacuum chamber. Therefore, in order to minimize the MP and resultant pressure rise in the vacuum chamber, it is important to carefully design the chamber or to utilize dampers for removing the unwanted resonant modes. The increases of secondary electron number with time are also shown in figure 10(b), where the temporal interval between two nearby peaks is approximately 0.22 ns (66 mm) corresponding to a half period of the resonant frequency of 2.3 GHz (0.44 ns, 132 mm). Thus, one can guess that from the chamber width of 66 mm, two-point MP by electron flight and collision between the vertical walls is dominant.

However, the particle tracking results in the vacuum chamber indicate that most secondary electrons originate individually from each vertical wall, as shown in figure 11(a). This means that the B-fields surrounding the E-fields in the TE mode are mainly responsible for the MP in the vacuum

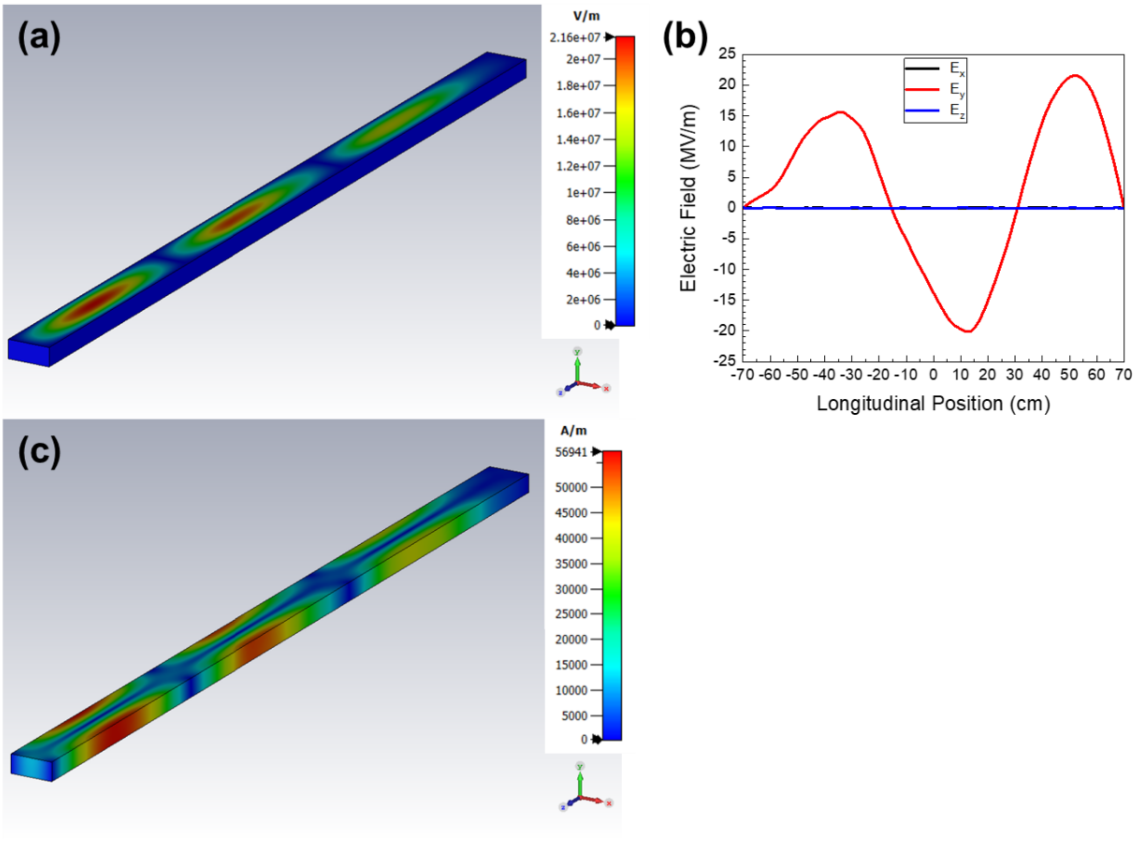

Figure 8. (a), (b) Electric field and (c) magnetic field distributions in the vacuum chamber with a resonant frequency of 2.3 GHz used for the MP analyses.

chamber. In other words, the initial low-energy electrons emitted from a vertical wall experience a cyclotron motion by B-fields, collide to another point on the same wall, and finally result in secondary electrons, which are much more than those by E-fields between the two horizontal walls. In static point of view, the E-fields in the TE mode are beneficial to the acceleration of electrons from a horizontal wall, but not to those from the opposite wall at the same time. Furthermore, the accelerated electrons might collide with those from the opposite wall and lose partial energies. The secondary electrons from the horizontal walls can also periodically experience deceleration after emission, be driven back to the emission surface, and be finally absorbed there [31]. Therefore, it is apparent that a main cause of the MP in the rectangular waveguide-like chamber is not E-fields but B-fields. Figure 11(b) shows a particle tracking result without mode resonance, where the emission of primary electrons are just shown. The emitted electrons will interact with particle beams passing through the chamber, however, the EM-fields by the beams are much lower than those from the mode resonance, which will be described in the next paragraph.

The electron MP phenomena can be expressed as the following equation in terms of time:

$$N(t) = N_0 e^{\alpha t}, \tag{2.1}$$

where $N(t)$ is a total electron number after a time t, N_0 an initial electron number, and α growth rate. Figure 12 shows the variation of the α with respect to the κ. Two input frequency ranges were

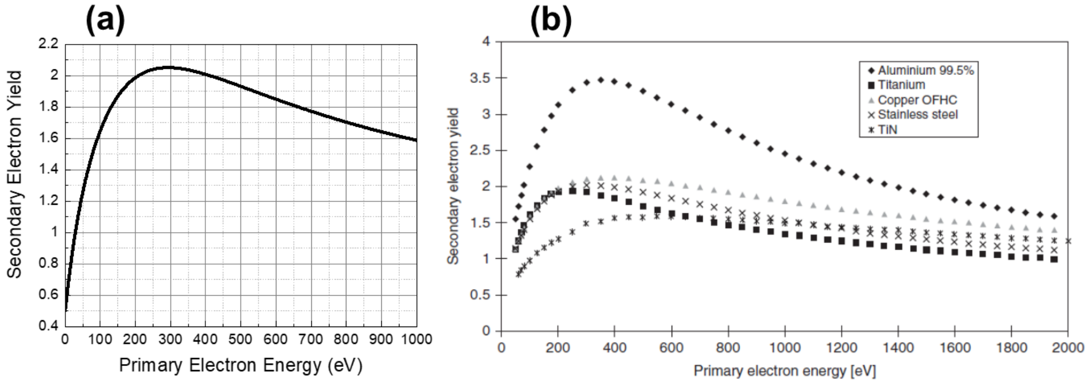

Figure 9. SEY curves of (a) Cu offered in the CST PS and (b) several materials in the literature. Source of (b): Malyshev 2020 [1], figure 8.16 (copyright 2020 Wiley-VCH) and Baglin et al. 2000 [30], figure 3 (copyright 2000, CERN).

examined in the simulations: one is narrow in 2–3 GHz and another is some broad in 1–6 GHz which is close to the mode frequency range in figure 6(a). The former resulted in the relatively more abrupt increase and gentle decrease, but the latter case was on the contrary and its maximum α was higher, as more clearly shown in the nonlinearly fitted data. One interpretation is that the multimode competition of 1–6 GHz slowly leads to higher maximum α and then abruptly decays without the lasting quasi-single mode contribution as in 2–3 GHz. It seems that the decay in high field region is resulted from both the SEY property with high-energy primary electrons and the near-confinement of secondary electrons by extremely strong B-fields at the vertical walls of the chamber. The nonlinearly fitted curve in 1–6 GHz (black bold and solid curve) is very similar to the pressure measurement ones seen in figure 2. As the κ corresponds to the average beam current, it is possible to conclude that in our case, the BIEM is covered with much stronger MP with mode resonance of the vacuum chamber. With a classical approach for ultra-relativistic charges in a cylindrical pipe of perfect conductor, an analytical estimation of the E-field by the 1 mA single bunch in the KARA electron storage ring is approximately 33.5 kV/m with beam parameters in table 2. However, in the fitted black solid curve of figure 12, the κ at the maximum α is ~3.3, which corresponds to an E-field of ~73 MV/m, where the κ of 1 represents ~22 MV/m, as shown in figure 8(b), with the stored energy of 1 J in the chamber. The amplified E-field can be calibrated by direct measurements in the resonant chamber. It has been reported that beam WFs could give rise to mode resonance of a vacuum chamber, where the peak E-fields were more than MV/m level [23, 24].

Similar MP simulations for vacuum chambers with different geometries have been performed. For a rectangular waveguide-like chamber with a height of 8 mm (a minimum gap of the SCU14) and the same other dimensions, no MP was foreseen, even though the same frequencies in both WFs and resonant TE modes exist in the chamber. The area reduction in the vertical walls seems to cause the decrease of secondary particles affected by B-fields. We also tried an elliptical vacuum chamber having dimensions of 33 and 14.5 mm in major and minor axes, respectively, with the same length of 1400 mm, similar to the rectangular chamber of $66 \times 29 \times 1400\ \mathrm{mm}^3$used in the main analyses, and the result was no MP as well. Although the both cases have not been experimentally verified, one can consider that a major factor causing the strong MP based on the mode resonance

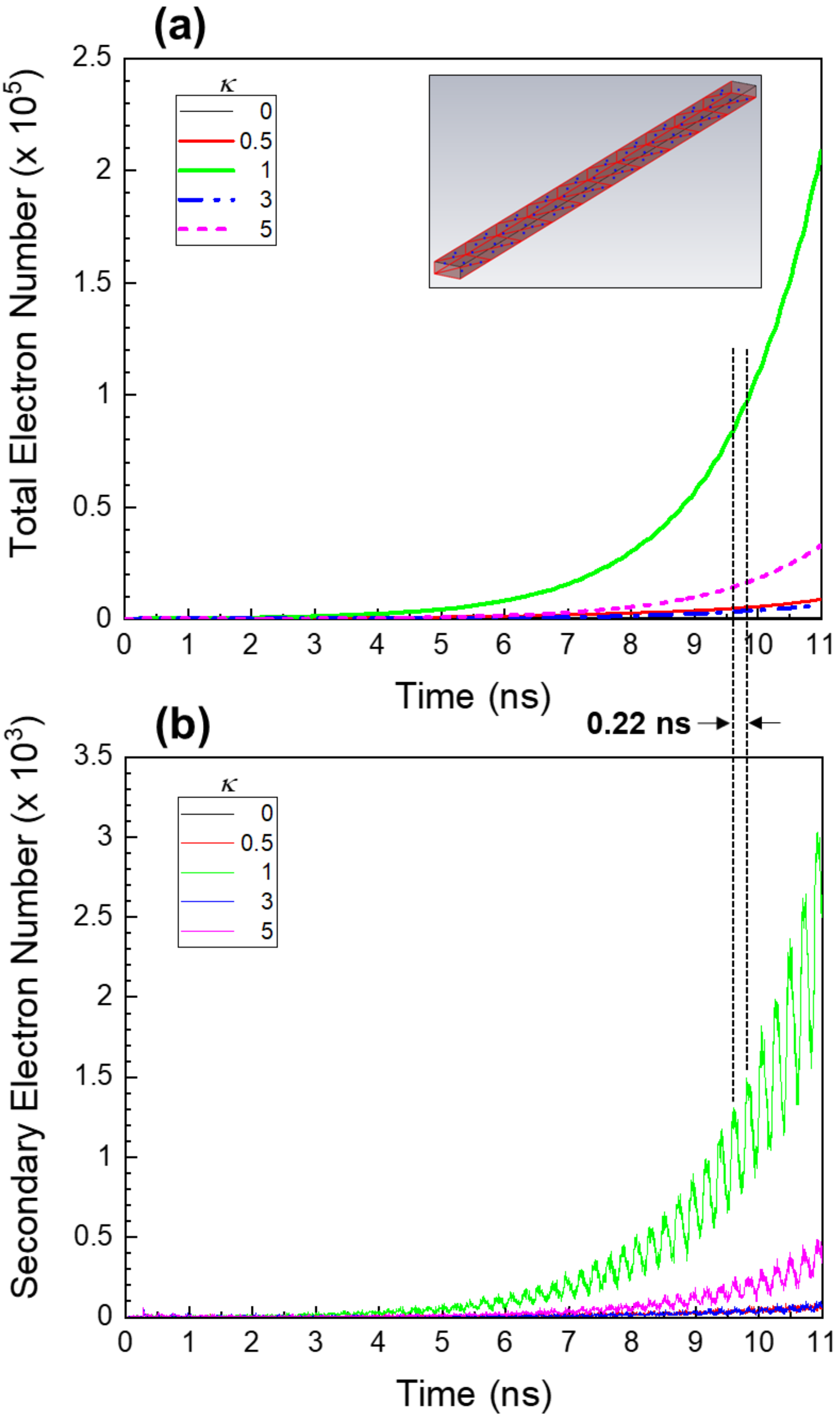

Figure 10. Variations of (a) total electron number and (b) secondary electron number, with time in the vacuum chamber. The scaling factor, κ corresponds to the electromagnetic field intensity. The inset in (a) shows 80 points for initial electrons emitted from four inner surfaces to simplify the MP simulations.

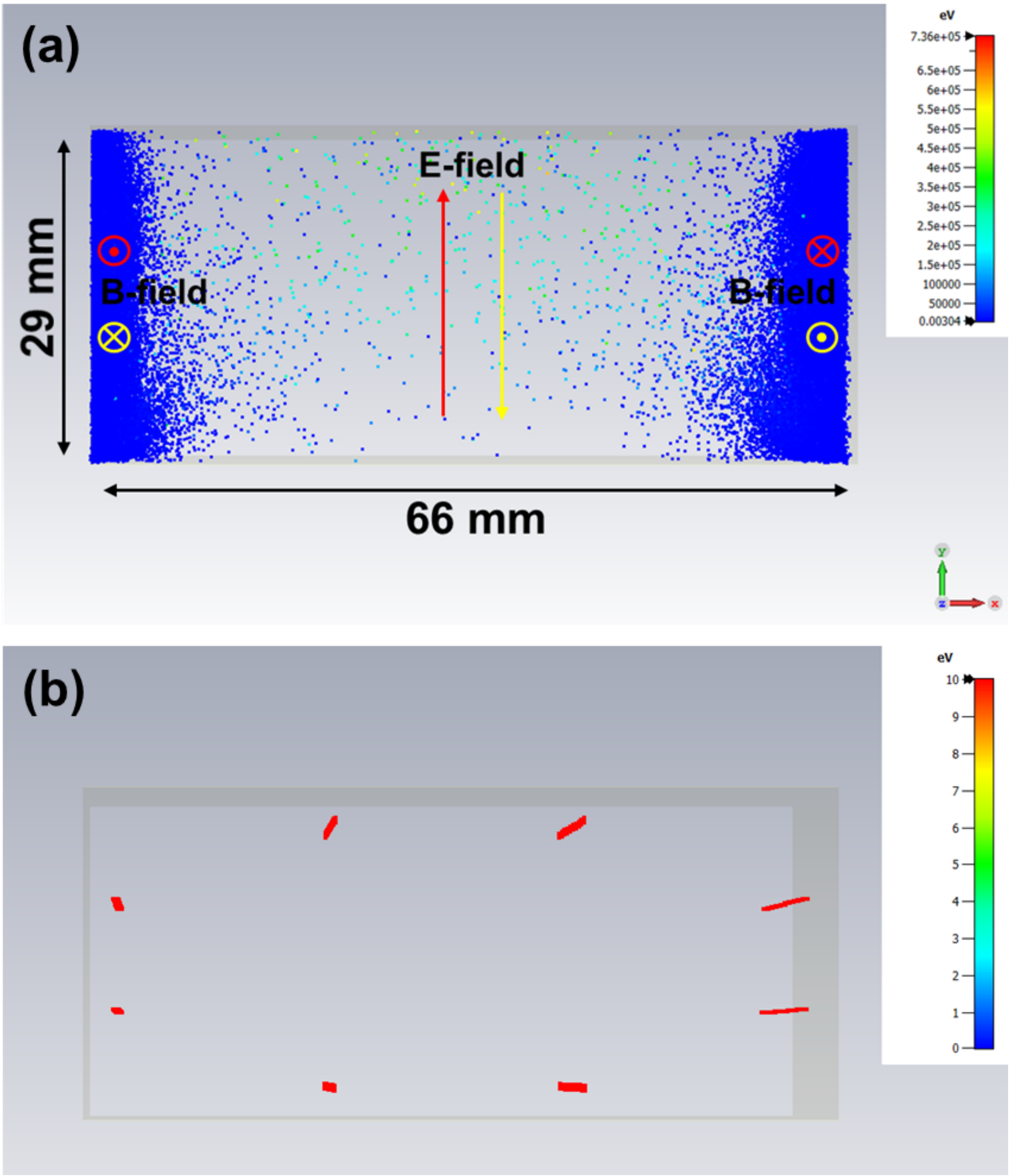

Figure 11. Transient particle tracking results (a) with and (b) without the mode resonance in the vacuum chamber. In (a), the dominant factor for much more secondary electrons is magnetic fields. In (b), the emission of primary electrons is just shown and there is no avalanche due to the absence of strong electromagnetic fields.

and the resultant pressure variation in a vacuum chamber is the chamber geometry itself, similar to the resonant RF devices. Figure 13 shows the E-field distributions in fundamental modes for the rectangular and elliptical vacuum chambers, respectively. In addition, the authors would like to remark that no pressure rise was observed and the absence of MP was proven by direct electron flux

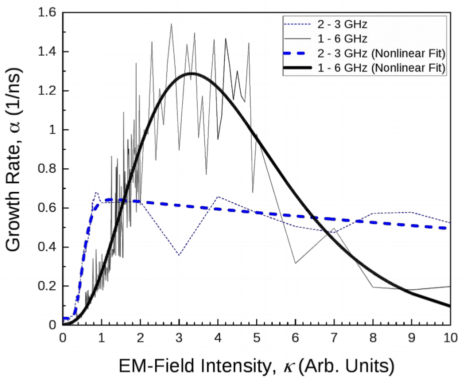

Figure 12. Variations of growth rate, α with electromagnetic field intensity, κ in different frequency ranges in the vacuum chamber. The κ of 1 represents the field intensity with the stored energy of 1 J in the chamber.

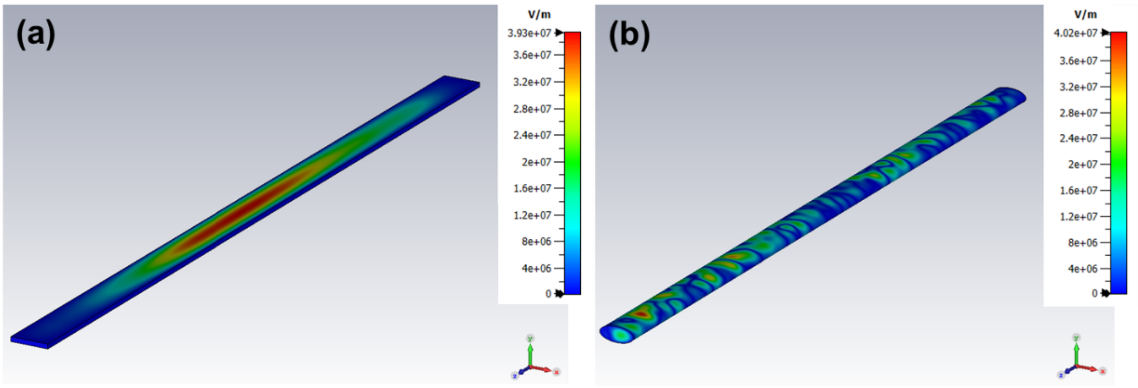

Figure 13. Electric field distributions in fundamental modes for (a) rectangular ($66 \times 8 \times 1400\,\text{mm}^3$) and (b) elliptical vacuum chambers (a major axis of 33 mm, a minor axis of 14.5 mm, and a length of 1400 mm), respectively.

measurements in warm and cold elliptical liners (Cu vacuum chambers) of the COLDDIAG (cold vacuum chamber for beam heat load diagnostics), developed at KIT, with electron beams at the DLS (Diamond Light Source) storage ring [32]–[34]. Our recent simulation results for the elliptical liner (a major axis of 30 mm, a minor axis of 5 mm, and a length of 490 mm) also showed no MP.

3 Discussion

The best way for validating the simulation results in figure 12 is to reproduce the pressure measurement curves in figure 2 from them. For this purpose, the κ band with positive α (0 to >10 in the fitted black solid curve) should match with the beam current range from ~80 or 110 mA to ~190 mA in the background vacuum of 10^{-10} mbar, under the assumption that the vacuum pressure is linearly dependent on the MP. The κ value at maximum α in figure 12 should be also coincident with one of the peak currents in figure 2. In this case, the EM-field intensities in figure 12 correspond to the average beam currents in figure 2, which means the amplification of WF to mode resonance. However, the nonlinear pressure curve always changed with a filling pattern of the KARA electron beam which affected to gas dynamic parameters such as composition and thickness of a cryosorbed layer in the vacuum chamber [20]. Meanwhile, the calculated EM-fields imported for the MP simulations originated from the eigenmodes in the chamber structure, regardless of beam parameters and filling patterns. Furthermore, the WF simulations were independently performed for just confirming the spectral coherence between the WF and the EM simulation results. Therefore, a direct comparison between the simulation and measurement results is unreasonable. As an alternative, heat loads by MP can be analytically calculated with the secondary electron energy gain and the number of colliding electrons per unit time (usually, several hours in gas dynamic analyses) and compared with measurement data of the heat loads. However, the MP simulation results showed the exponential growth of particle number in a time scale of nano-seconds, where the final electron number depends on the initial emission parameters such as the number and kinetic energy of primary electron bunches from the material. Thus, it is also very difficult to estimate the MP-based heat loads from the simulation results. If the EM-field intensities in the resonant vacuum chamber are measured with changing the beam current and the filling pattern, the correspondence between the simulation and measurement results might be verified. The pressure measurements were performed in 2007 and unfortunately, the present status is that the SCU14 was completely removed from the KARA storage ring.

Nevertheless, this scenario is the only way to explain the explosive pressure variation observed at relatively lower beam currents in the electron machine. Under such a postulate of the MP with mode resonance, the introduction of a big aperture for decreasing the collision number of secondary electrons between the chamber walls can be not beneficial to the suppression of “total” MP, differently from the classical beam-induced approach. It is also believed that coupled EM and MP analyses for vacuum chambers make it possible to predict the existence of strong MP with mode resonance characterized by the chamber geometry.

4 Conclusions

Simulation results on strong electron MP with mode resonance were presented to explain the significant pressure variation measured in a cryogenic vacuum chamber of the KARA electron storage ring. Through the numerical analyses, the spectral coherence between the WFs and the eigenmodes in the chamber was verified and the measured pressure nonlinearity was theoretically reproduced. In addition, the secondary electron motion in a relatively much shorter time scale in contrast to that in the previous gas dynamic studies could be understood. The theoretical connection of the WFs with the mode resonance in terms of a beam parameter and a filling pattern is still a subject to resolve.

Acknowledgments

H.J. Cha would like to acknowledge the discussion with S. Casalbuoni. This work was supported by the BMBF project 05H18VKRB1 HIRING (Federal Ministry of Education and Research) in Germany.

References

[1] O.B. Malyshev, *Vacuum in particle accelerators*, Wiley-VCH, Weinheim Germany (2020).

[2] K. Ohmi and F. Zimmermann, *Head-tail instability caused by electron cloud in positron storage rings*, *Phys. Rev. Lett.* **85** (2000) 3821.

[3] O.S. Bruning et al., *LHC Design Report. Volume 1: The LHC Main Ring*, in *CERN Yellow Reports: Monographs*, CERN, Geneva Switzerland (2004) [CERN-2004-003-V-1].

[4] F. Zimmermann, *Review of single bunch instabilities driven by an electron cloud*, *Phys. Rev. Spec. Top. Accel. Beams* **7** (2004) 124801.

[5] M. Zobov et al., *Operating experience with electron cloud clearing electrodes at DAFNE*, in proceedings of the *5th Workshop on Electron-Cloud Effects (ECLOUD'12)*, La Biodola, Italy, 5–9 June 2012, *Conf. Proc. C* **1206051** (2013) 259 [`arXiv:1306.5944`].

[6] G. Rumolo, F. Zimmermann, H. Fukuma and K. Ohmi, *Electron cloud studies for KEKB*, in proceedings of the *19th IEEE Particle Accelerator Conference (PAC 2001)*, Chicago, IL, U.S.A., 18–22 June 2001, pp. 1889–1891 [*Conf. Proc. C* **0106181** (2001) 1889] [CERN-SL-2001-040-AP].

[7] E. Belli, M. Migliorati and G. Rumolo, *Electron cloud and collective effects in the interaction region of FCC-ee*, in proceedings of the *58th ICFA Advanced Beam Dynamics Workshop on High Luminosity Circular e^+e^- Colliders (eeFACT2016)*, Daresbury, U.K., 24–27 October 2016, pp. 130–135 [eeFACT-2016-TUT3AH7].

[8] O. Gröbner, *Beam induced multipacting*, *Conf. Proc. C* **970512** (1997) 3589 [CERN-LHC-PROJECT-REPORT-127].

[9] F. Zimmermann, *A simulation study of electron-cloud instability and beam-induced multipacting in the LHC*, LHC-Project-Report-95 (1997) [CERN-LHC-Project-Report-95] [SLAC-PUB-7425].

[10] J.R. Calvey, W. Hartung, J. Makita and M. Venturini, *Beam induced electron cloud resonances in dipole magnetic fields*, *Phys. Rev. Accel. Beams* **19** (2016) 074401 [`arXiv:1603.04817`].

[11] E. Somersalo, P. Ylä-Oijala, D. Proch and J. Sarvas, *Computational methods for analyzing electron multipacting in RF structures*, *Part. Accel.* **59** (1998) 107.

[12] H.J. Cha, J. Yoon, S.W. Jang, K.-R. Kim, S.H. Park and E.-S. Kim, *Design of a balloon-shaped superconducting single spoke resonator*, *J. Korean Phys. Soc.* **75** (2019) 117.

[13] S. Papadopoulos et al., *Experience with the conditioning of Linac4 RF cavities*, in proceedings of the *28th Linear Accelerator Conference (LINAC2016)*, East Lansing, MI, U.S.A., 25–30 September 2016.

[14] S. Casalbuoni, S. Schleede, D.S. de Jauregui, M. Hagelstein and P.F. Tavares, *Can electron multipacting explain the pressure rise in a cold bore superconducting undulator?*, *Phys. Rev. Spec. Top. Accel. Beams* **13** (2010) 073201.

[15] F. Zimmermann, *The electron cloud instability: Summary of measurements and understanding*, in proceedings of the *2001 Particle Accelerator Conference (PAC2001)*, Chicago, IL, U.S.A., 18–22 June 2001, pp. 666–670 [*Conf. Proc. C* **0106181** (2001) 666] [CERN-SL-2001-035-AP].

[16] A. Kulikov, A. Novokhatski and J. Seeman, *Suppression of the beam instability related to electron cloud at PEP-II B-factory*, SLAC-PUB-10886 (2004).

[17] M.S. Zisman and T.M. Himel, *Commissioning of the PEP-II low-energy ring*, in proceedings of the *1999 Particle Accelerator Conference (PAC'99)*, New York, NY, U.S.A., 29 March–2 April 1999, pp. 293–295 [SLAC-REPRINT-1999-060].

2021 JINST 16 P11001

[18] A. Kulikov et al., *The electron cloud instability at PEP-II*, in proceedings of the *2001 Particle Accelerator Conference (PAC2001)*, Chicago, IL, U.S.A., 18–22 June 2001, pp. 1903–1905 [*Conf. Proc. C* **0106181** (2001) 1903] [SLAC-PUB-9428].

[19] A. Kulikov, J. Seeman and S. Heifets, *Current dependent pressure rise at PEP-II LER*, SLAC-PUB-8227 (1999).

[20] S. Casalbuoni et al., *Beam heat load and pressure rise in a cold vacuum chamber*, *Phys. Rev. Spec. Top. Accel. Beams* **10** (2007) 093202.

[21] R. Dowd, M. Atkinson, M. Boland, G. LeBlanc, Y.R. Tan and D. Teytelman, *Investigation of trapped resonant modes in insertion devices at the Australian synchrotron*, in proceedings of the *7th International Particle Accelerator Conference (IPAC2016)*, Busan, Korea, 8–13 May 2016.

[22] Y. Kang, G. Decker and J. Song, *Damping spurious harmonic resonances in the APS storage ring beam chamber*, in proceedings of the *1999 Particle Accelerator Conference (PAC'99)*, New York, NY, U.S.A., 29 March–2 April 1999, pp. 3092–3094.

[23] Y. Joo, I.-M. Hwang, S.-J. Park and C. Kim, *Measurement of resonance modes causative of beam position monitor signal noise in vacuum chamber of storage ring*, *Nucl. Instrum. Meth. A* **638** (2011) 11.

[24] R. Kustom, J. Bridges, W. Chou, J. Cook, G. Mavrogenes and G. Nicholls, *Analysis of RF Modes in the ANL APS Vacuum Chamber Using Computer Simulation, Electron Beam Excitation and Perturbation Techniques*, in proceedings of the *1989 Particle Accelerator Conference (PAC'89)*, 20–23 March 1989, Chicago, IL, U.S.A., pp. 1755–1757 [*Conf. Proc. C* **8903201** (1989) 1755] [CONF-890335-200].

[25] Y. Shobuda, Y.H. Chin and K. Takata, *Coupling impedances of a gap in vacuum chamber*, *Phys. Rev. Spec. Top. Accel. Beams* **10** (2007) 044403.

[26] NIST, *Properties of solid materials from cryogenic- to room-temperatures*, (2021) https://trc.nist.gov/cryogenics/materials/materialproperties.htm.

[27] A. Papash et al., *New operation regimes at the storage ring KARA at KIT*, in proceedings of the *10th International Particle Accelerator Conference (IPAC2019)*, Melbourne, Australia, 19–24 May 2019.

[28] S. Shee and S. Dwivedi, *Design and simulation study of double side-cavity gridless reltron with dual extraction sections*, *J. Electromagn. Waves Appl.* **35** (2020) 291.

[29] A. Kuzucan, *Secondary electron yield on cryogenic surfaces as a function of physisorbed gases*, Ph.D. Dissertation, Vienna University of Technology, Vienna Austria (2011).

[30] V. Baglin et al., *The secondary electron yield of technical material and its variation with surface treatments*, in proceedings of the *7th European Particle Accelerator Conference (EPAC 2000)*, Vienna, Austria, 26–30 June 2000, CERN-LHC-PROJECT-REPORT-433 (2000).

[31] R.L. Geng, H. Padamsee and V. Shemelin, *Multipacting in a Rectangular Waveguide*, in proceedings of the *2001 Particle Accelerator Conference (PAC2001)*, Chicago, IL, U.S.A., 18–22 June 2001, pp. 1228–1230 [*Conf. Proc. C* **0106181** (2001) 1228] [SRF-010723-07].

[32] S. Casalbuoni, M. Migliorati, A. Mostacci, L. Palumbo and B. Spataro, *Beam heat load due to geometrical and resistive wall impedance in COLDDIAG*, 2012 *JINST* **7** P11008.

[33] S. Gerstl et al., *Cold vacuum chamber for diagnostics: Instrumentation and first results*, *Phys. Rev. Spec. Top. Accel. Beams* **17** (2014) 103201.

[34] R. Voutta et al., *Cold vacuum chamber for diagnostics: Analysis of the measurements at the Diamond Light Source and impedance bench measurements*, *Phys. Rev. Accel. Beams* **19** (2016) 053201.